Dalton Transactions

Site Specific Redox Properties in Ligand Differentiated Di-Nickel Complexes Inspired by the Acetyl CoA Synthase Active Site

Journal:	*Dalton Transactions*
Manuscript ID	DT-ART-01-2024-000306.R1
Article Type:	Paper
Date Submitted by the Author:	15-Mar-2024
Complete List of Authors:	Quiroz, Manuel; Texas A&M University College Station, Chemistry Jana, Manish; Texas A&M University, Chemistry Liu, Kaiyang; UCLA Bhuvanesh, Nattamai; Texas A&M University, Department of Chemistry Hall, Michael; Texas A&M University, Chemistry Darensbourg, Marcetta; Texas A&M Univ, Chemistry

Site Specific Redox Properties in Ligand Differentiated Di-Nickel Complexes Inspired by the Acetyl CoA Synthase Active Site

Manuel Quiroz, Manish Jana, Kaiyang Liu, Nattamai Bhuvanesh, Michael B. Hall,

and Marcetta Y. Darensbourg *

Department of Chemistry, Texas A & M University, College Station, Texas 77843, United States

Abstract: Bimetallic transition metal complexes with site-specific redox properties offer a versatile platform for understanding electron polarization, intramolecular electron transfer processes, and customizing electronic and magnetic properties that might impact reactivity and catalyst design. Inspired by the dissymmetric nickel sites in the Acetyl CoA Synthase (ACS) Active Site, three new bimetallic $Ni(N_2S_2)$-$Ni(S_2C_2R_2)$ complexes based on $Ni(N_2S_2)$ metalloligand donor synthons, Ni_d, in mimicry of the nickel site distal to the redox-active iron sulfur cluster of ACS, and nickel dithiolene receiver units, designated as Ni_p, , the nickel proximal to the 4Fe4S cluster, were combined to explore the influence of ligand environment on electronic structure and redox properties of each unit. The combination of synthons gave a matrix of three S-bridged dinickel complexes, characterized by x-ray crystallography, and appropriate spectroscopies. Computational modeling is connected to the electronic characteristics of the nickel donor and receiver units. This study demonstrated the intricacies of identifying sites of electrochemical redox processes, within multi-metallic systems containing non-innocent ligands.

Introduction

The positioning of two metal centers in proximity allows for synergistic effects, where the redox properties of one metal can activate the other, or both metals may share the burden of charge

accumulation. This cooperative behavior enables the development of catalysts with tailored reactivity, leading to improved reaction rates and selectivity compared to individual metal complexes.[1-4] The redox potential of each metal is largely tuned by the coordination environment that can be leveraged towards site selective redox chemistry on a targeted metal. Such an approach has led to a wide range of reactions and applications, including C-C cross-coupling, hydrogenation, nitrogen activation, and carbon-heteroatom bond formation.[5-7]

A biological exemplar of this phenomenon exists in the active site of the (ACS)/(CODH) complex found in acetogenic bacteria. This assembly performs the catalytic conversion of CO, CH_3^+, and Coenzyme-A fragments into Acetyl-Coenzyme A (Acetyl-CoA), akin to the industrial Monstanto Process.[8-11] **Figure 1** depicts the active site of ACS known as the A-Cluster, which consists of two distinct nickel centers bridged to a conventional 4Fe4S cluster by a cysteinyl thiolate. The nickel center (Ni_d) that is positioned distally from the 4Fe4S cluster, Ni_d, adopts a square planar configuration facilitated by the tripeptide Cys-Gly-Cys (CGC)-based N_2S_2 motif. For synthetic chemistry, the Ni(CGC) acts as a metallodithiolateligand to a second catalytically active nickel, referred to as Ni_p; i.e., Ni_p is proximal to the 4Fe4S cluster. The Ni_p is coordinated

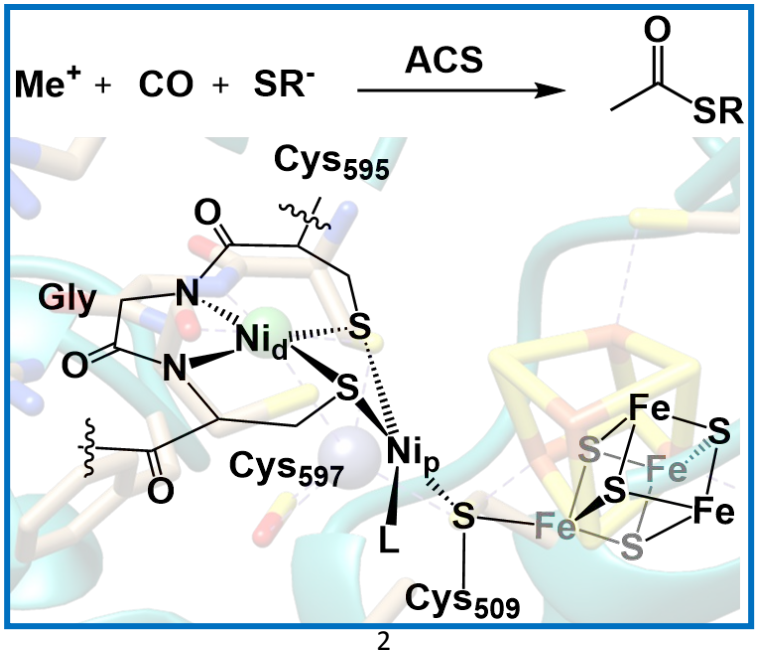

Figure 1. Active site of Acetyl CoA synthase.[8-11]

by three bridging thiolates in its resting state: two originate from the Ni(CGC) and one from a cysteine residue that bridges Ni_p to the 4Fe4S cluster. While Ni_d occupies a tightly bound site within the CGC motif, nature has fine-tuned the ligand environment such that Ni_p exhibits greater flexibility with changes in redox levels, expected to be facilitated by the redox-active iron sulfur cluster during catalysis.[8-11]

Our primary objective was to create a platform specifically tailored for integrating redox preferentiality into dinickel complexes related to the ACS active site. By doing so, we aimed to gain a comprehensive understanding of how different coordination environments impact the redox properties of these complexes. In this regard neutral Ni(N_2S_2) complexes have been developed as metalloligands donors towards many secondary receiving metals units, generating a wealth of multimetallic and bimetallic architectures.[12] Recently, we showed the advantages of using nickel dithiolene as a receiving unit that imparted rich magnetic and redox properties within an (N_2S_2)iron nitrosyl – nickel dithiolene complex.[13] Using a similar strategy, we have prepared NiNi' complexes with varying Ni(N_2S_2) donors and nickel dithiolene receivers (Ni') to generate a series informative on site specific redox chemistry. Incorporating the dithiolene offers the additional advantage of an electron reservoir, analogous to the redox-active 4Fe4S cluster bridged to Ni_p, a feature not observed in any ACS model compound to date.[14-17] The new dinickel complexes underwent comprehensive characterization using multiple analytical techniques, including X-ray crystallography, UV−vis spectroscopy, EPR spectroscopy, Cyclic Voltammetry, and ^{1}H-NMR spectroscopy. Additionally, computational studies were conducted to validate the essential electronic properties governing oxidation and reduction.

Results and Discussion

Synthesis

Developed by Donahue, *et al*., the $Ni(S_2C_2R_2)(CNMe)_2$ ($[S_2C_2(CN)_2]^{2-}$ = maleonitriledithiolate "mnt" or $[S_2C_2(Ph)_2]^{2-}$ = 1,2-diphenyl-1,2-dithiolate "dpdt") were used as entry synthons towards heteroleptic nickel dithiolene complexes. [18,19] The $Ni(N_2S_2)$-$Ni(S_2C_2R_2)$ complexes (where, N_2S_2 = *N,N'*-dimethyl-*N,N'*-bis(2-mercaptoethyl)ethylenediamine "bme-dame" or *N,N'*-ethylenebis(mercaptoacetamide) "ema") were prepared by adding the $Ni(N_2S_2)$ complexes[20,21] as S-donors to the $Ni(S_2C_2R_2)(CNMe)_2$ synthons, **Figure 2b**. The metallodithiolates displaced the methyl isocyanide ligands as evidenced by concomitant decrease of the CΞN symmetric and antisymmetric bands of the $Ni(S_2C_2R_2)(CNMe)_2$ starting material, and the isolation of crystalline products in good yield.

The reaction conditions of Ni(bme-dame) and $[Ni(ema)]^{2-}$ with Ni(dpdt) leading to Ni(bme-dame)-Ni(dpdt) and $[Ni(ema)\text{-}Ni(dpdt)]^{2-}$, complex **1** and $\mathbf{2^{2-}}$, respectively, varied drastically. That is, the former $Ni(N_2S_2)$ donor required heating overnight while the latter reaction was complete within 15 mins at room temperature. This reflects the donor ability of each $Ni(N_2S_2)$, where the dianion $[Ni(ema)]^{2-}$ is a stronger nucleophile than neutral Ni(bme-dame), resulting in lower activation barriers for methyl isocyanide ligand displacement. The electronic character of the nickel-dithiolene receiver group also affected the reaction conditions. The electron withdrawing cyano groups in $Ni(mnt)(CNMe)_2$ resulted in shorter reaction times at ambient temperatures with Ni(bme-dame) to form Ni(bme-dame)-Ni(mnt), complex **3**. The $[Ni(ema)\text{-}Ni(mnt)]^{2-}$ complex could not be isolated due to the additional displacement of $(mnt)^{2-}$ by $[Ni(ema)]^{2-}$ to generate the known trimetallic $[Ni(ema)\text{-}Ni^{II}\text{-}Ni(ema)]^{2-}$ complex, detected by ESI-MS.

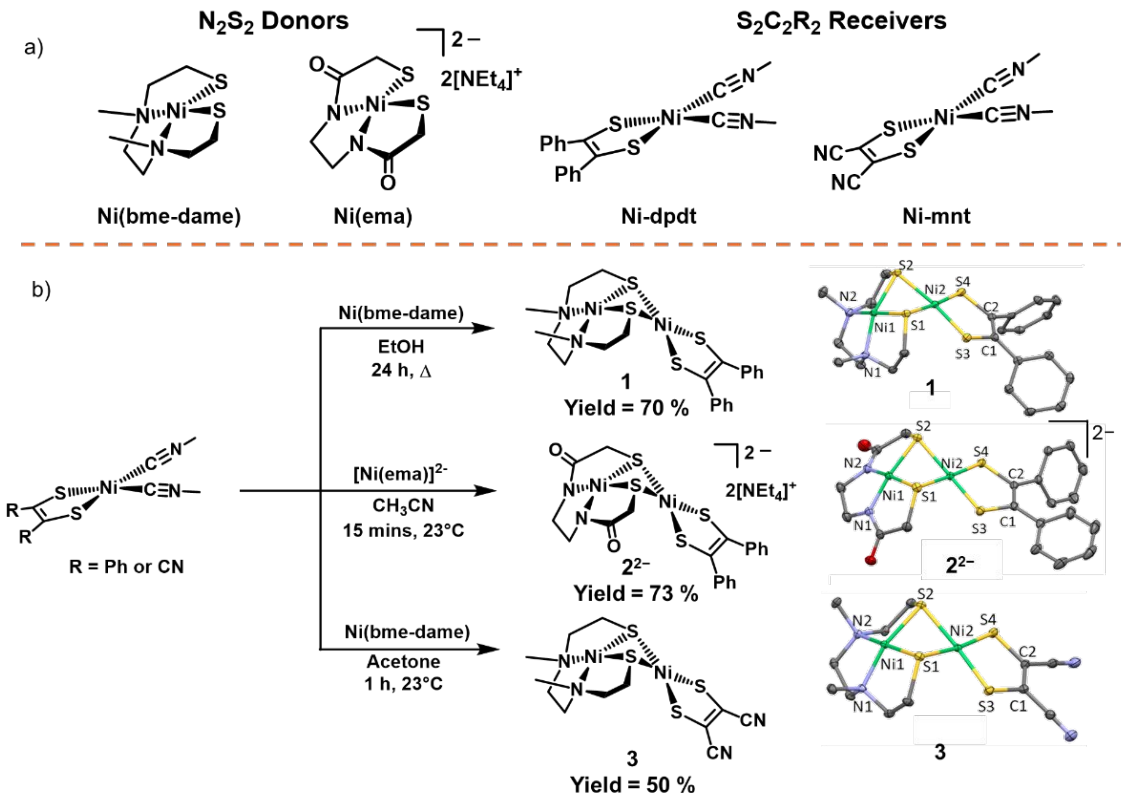

Figure 2. a) Synthons used in the preparation of the S-bridged, dissymmetric di-nickel complexes for this study. **B)** Preparation and XRD structures of the di-nickel complexes **1**, Ni(bme-dame)-Ni(dpdt); $\mathbf{2}^{2-}$, [Ni(ema)-Ni(dpdt)][Net_4]$_2$ **;** and **3**, Ni(bme-dame)-Ni(mnt).

All products are dark red, diamagnetic solids with sharp ^{1}H NMR signals (see ESI **Figures S1-3**): the data are consistent with two square planar Ni(II) centers. Neutral complexes **1** and **3** are air stable as solids or in solution while dianionic complex $\mathbf{2}^{2-}$ rapidly degrades in air. X-ray diffraction quality crystals of **1** were obtained at −35 °C in DCM/hexane mixture, whereas crystals of $\mathbf{2}^{2-}$ were obtained in CH_3CN layered with ether at −35 °C. Due to poor solubility, crystals of **3** were grown in DMSO layered with a 50/50 mixture of H_2O/MeOH at 23 °C.

X-ray diffraction analysis

The molecular structures of **1**, $\mathbf{2}^{2-}$ and **3** are rendered in **Figure 2** as chem draw graphics and thermal ellipsoid plots. Selected metric parameters are tabulated in **Table 1**. The bidentate binding

of the cis-dithiolates towards the nickel-dithiolene units gives the characteristic hinged or "butterfly" -like structure for each complex. In comparison to the isolated, unbound NiN_2S_2 metallodithiolate ligands the ∠S-Ni-S bite angles within the dinickel complexes are contracted by *ca.* 7° to 9°. A significant displacement of the Ni1 from the best N_2S_2 plane of the binding is also observed for all complexes (**1**, $\mathbf{2}^{2-}$ and **3**) compared to the free NiN_2S_2 metallodithiolate ligands.

The angle of intersection (hinge angle) of the mean N_2S_2 and S_4 planes ranges from 102.5° to 111.6°and is in the order of **1** > $\mathbf{2}^{2-}$ > **3**. The sums of the covalent atomic radii of Ni/Ni', and the Ni1-Ni2 distances of 2.72, 2.68, and 2.78 Å for **1**, $\mathbf{2}^{2-}$, and **3**, respectively, are inconsistent with metal-metal bonding. While one would expect that the Ni1-Ni2 distance would increase with wider hinge angles, the data for complex $\mathbf{2}^{2-}$ does not comply with this assumption. This likely results from the Ni displacement from the mean N_2S_2 plane ($Ni1_{disp}$), see Table **1**. We conclude that the variation in structural parameters between the free NiN_2S_2 metalodithiolate ligand vs bound NiN_2S_2•$NiS_2C_2R_2$ units reflect a combination of factors from the geometrical preferences for Ni^{2+} in attempts to find the optimal orientation of the sulfur lone pairs to bind the second nickel. Structural examination of the nickel-dithiolene unit informs on the well-documented, non-innocent nature of metal dithiolenes, specifically, the S-C and C-C distances of the dithiolene. The S3-C2 and S4-C1 distances, numbered scheme as shown in **Figure 2**, for **1**, $\mathbf{2}^{2-}$, and **3** are similar ranging from 1.74 to 1.77 Å with C1-C2 distances ranging from 1.34 to 1.36 Å. These distances suggest that the dithiolene in all three exists as di-anionic, ene-1,2-dithiolate, resembling the homoleptic $[Ni(S_2C_2Me_2)_2]^{2-}$ that has average S-C and C-C distances of 1.76 Å and 1.34 Å, respectively.[22,23]

Table 1. Comparison of structural metric parameters of complexes **1**, $\mathbf{2^{2-}}$, and **3**.

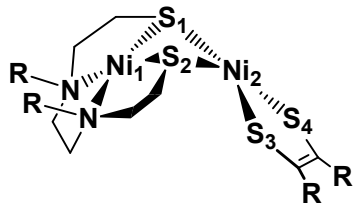

Distances (Å)	**1**	$\mathbf{2^{2-}}$	**3**
Ni1–Ni2	2.7202(5)	2.6885(6)	2.7871(3)
S3–C1	1.766(2)	1.772(2)	1.738(2)
S4–C2	1.764(2)	1.760(2)	1.737(1)
C1–C2	1.348(3)	1.356(2)	1.361(2)
$Ni1_{disp}$ [a] *($Ni1_{disp}$ for free ligand [a])*[20,21]	0.250 *(0.003)*	0.150 *(0.027)*	0.207 *(0.003)*
$Ni2_{disp}$ [b]	0.01	0.06	0.04
τ_4 (NiN_2S_2) *(τ_4 (NiN_2S_2) for free ligand)*[20,21]	0.20 *(0.13)*	0.13 *(0.09)*	0.17 *(0.13)*
Angles			
S1–Ni1–S2 *(S1-Ni1-S2 for free ligand)*[20,21]	85.32(2) *(93.99)*	90.18(2) *(97.47)*	86.36(3) *(93.99)*
S1–Ni2–S2	81.64(2)	83.80(2)	82.26(3)
S1–Ni2–S3	92.33(2)	91.24(2)	92.24(1)
S2–Ni2–S4	94.94(2)	94.00(2)	92.14(1)
S3–Ni2–S4 *(S3-Ni2-S4 for free ligand)*[20,21]	91.22(2) *(90.03)*	90.81(2) *(90.03)*	93.39(2) *(92.80)*
Hinge 1 [c]	102.53	110.37	111.69
Hinge 2 [d]	111.82	114.08	117.98
Space Group	$P2_1/n$	$P\bar{1}$	$P\bar{1}$

[a] The distance between Ni1 and the mean plane of the N_2S_2 ligand.
[b] The distance between Ni2 and the mean plane of the S_4 plane.
[c] Hinge angle of intersection between the S-Ni1-S and S-Ni2-S
[d] Hinge angle of intersection between the mean plane of the N_2S_2 and S_4 planes.

Electrochemical Studies

The electrochemical behaviors of the complexes in solution were investigated by cyclic voltammetry (CV) in attempts to establish the effect(s) of donor and receiver nickel units on the electronic properties of the bimetallics. Cyclic voltammograms of **1**, $\mathbf{2}^{2-}$, and **3** were recorded in CH_3CN solutions containing 0.1 M $[^tBu_4N][PF_6]$ as the supporting electrolyte at room temperature under argon and referenced to $Fc^{+/0}$ ($E_{1/2}$ = 0.0 V) as an internal standard, **Figure 3**. The observable redox waves for complex **1**, at E_{pa} = −0.32 V (E_{pc} = −0.41 V) and −1.79 V (E_{pc} = −1.87 V), show a linear dependence of current with respect to square root of scan rate (see ESI, **Figure S10A**). The difference in slopes lead to the conclusion that the integrated area of the electron transfer coefficient alpha does not track with scan rate (See ESI, **Figure S10B**). As the scan rate increases, the electron transfer rate becomes significantly higher than the diffusion rate, and the rate-determining step changes from the mass transfer process to the charge transfer process. For complex $\mathbf{2}^{2-}$, a similar quasi-reversible redox event at E_{pa} = −0.58 V (E_{pc} = −0.64V) was observed (**Figure 3**); plots of current with respect to the square root of scan rate also show different slopes (see ESI, **Figure S13**).

Heteroleptic nickel dithiolene complexes that feature a $Ni(S_2C_2Ph_2)$ unit[18,19] have been shown to have reversible oxidation events that are primarily dithiolene ligand based, including our recently studied $(NO)Fe(N_2S_2)$-$[Ni(S_2C_2Ph_2)]$ which displayed a $E_{1/2}$ of −0.24 V.[13] The redox potential of the $[Ni(S_2C_2Ph_2)]^{+/0}$ couple in the current study is expected to depend on the donation of the MN_2S_2 donor units. That is, the neutral $Ni(N_2S_2)$ is a slightly better donor than $(NO)Fe(N_2S_2)$, leading to a negative shift in oxidation potential (assigned to dithiolene based redox event, DT in **Figure 3**) of *ca.* 0.14 V. However, donation from the dianionic $[Ni(ema)]^{2-}$ is much greater compared to neutral Ni(bme-dame) ligand, yielding a more negative shift in oxidation

potential (*ca.* 0.24 V) than the neutral Ni(bme-dame) metallo ligand. It should be emphasized that the shift in the dithiolene based redox event is a result of the electron donor ability of the MN_2S_2.

At this point we must mention that the non-innocent character of the dithiolene ligand has led us to diversify designations of the two nickels sites in the bimetallic. It is our intention to include the ligand fields, especially the dithiolene ligand itself, as primary location of electrochemical changes-rather than the actual nickel atom which holds its position relative to the second nickel. In this regard, we call on the designations accepted for the enzyme active site, Ni_d and Ni_p. The nickel proximal to the active site and its attachment to the ultimate redox active center, 4Fe4S cluster, is most relatable to our Ni2 and will occasionally be designated as Ni_p, in reference to the redox activity of the unit.

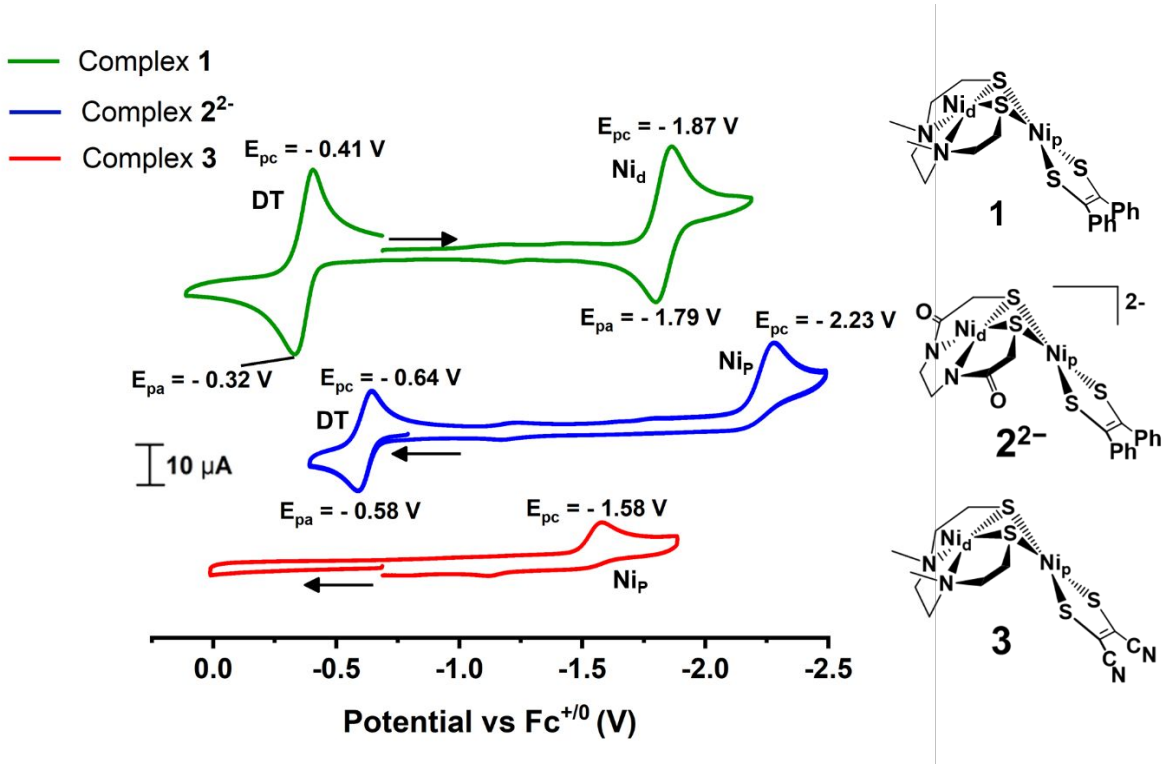

Figure 3. Cyclic voltammograms of compounds **1** (green), $\mathbf{2}^{2-}$ (blue), and **3** (red) at a scan rate of 100 mVs^{-1} in CH_3CN and referenced versus $Fc^{+/0}$. The Ni within the N_2S_2 ligation emulates the distal nickel of the ACS active site, Ni_d; the Ni closer to the iron sulfur cluster, Ni_p, is in the NiS_4 binding site; and the DT designation in the model refers to a largely dithiolene based redox event.

*Assignments of the more negative redox events for complexes **1** and **2**$^{2-}$ and the single redox event of **3**:*

The single redox event of **3** in this potential window (0 to −2.5 V), was verified in multiple batches of samples; its position is likely due to the electron-withdrawing effect of the cyano group on the Ni($S_2C_2(CN)_2$) unit signaling difficulty in electron removal (oxidation) from the dithiolene unit. This presumably reflects an electron-deficient 4Fe4S cluster in the ACS active site.

The CV scans in the cathodic direction show quasi-reversible events for **1** at E_{pc} = −1.87 V and irreversible reductions of **2**$^{2-}$ and **3** at −2.23 V and −1.58 V, respectively. Increasing scan rates at these potentials produce improved reversibility for **1** however **2**$^{2-}$ and **3** stay irreversible. The irreversibility is attributed to geometric changes upon reduction, consistent with the computational results (discussed later). Neutral Ni(N_2S_2) complexes, varying only by the N to N and N to S hydrocarbon connectors, have reduction potentials at *ca.* –2.4 V for the $Ni^{II/I}$ couple which is known to shift up to 700 mV anodically when bound to a second metal.[24] In this context, the reduction of **1** falls within the range for a Ni(N_2S_2) based reduction while the reduction potential for **3** is too positive even when considering its attachment to the more electron-withdrawing Ni(mnt) receiver unit. *Therefore, we posit that the event at −1.58 V signals reduction of the dinickel complex **3** is at the Ni(mnt) unit, which we assert is analogous to the proximal nickel of the ACS active site, Ni_p.* Conversely, the $[Ni(ema)]^{2-}$ as its salt, does not have a $Ni^{II/I}$ redox couple within the solvent window and only appears when bound to a second metal, in which its charge is ameliorated.[24] For example, in the case of the $[Ni(ema)\text{-}W(CO)_4]^{2-}$ bimetallic complex, a $Ni^{II/I}$ reduction was observed at −2.74 V.[24] Thus, the 510 mV difference between the Ni-W complex and **2**$^{2-}$ suggests that the $Ni^{II/I}$ reduction at −2.23 V should be based on the dithiolene unit of Ni(dpdt). In the more anodic region (see ESI, **Figure S11**), several irreversible oxidations are

present that are likely sulfur-based, coming from the N_2S_2 ligand, and lead to degradation of the bimetallics. Full scans and scan rate dependence of **1**, $\mathbf{2}^{2-}$ and **3** are given in the ESI (**Figures S8-14)**.

Computational Studies

To further support the redox assignments made from the electrochemical studies of these complexes, density functional theory (DFT) analyses were performed with the SMD solvation model (acetonitrile) using the functional/basis set TPSS/6-311++G(d,p) for all atoms (see experimental section for details). This functional has performed particularly well for prediction of structures and electrochemical properties of similar complexes.[25-28]

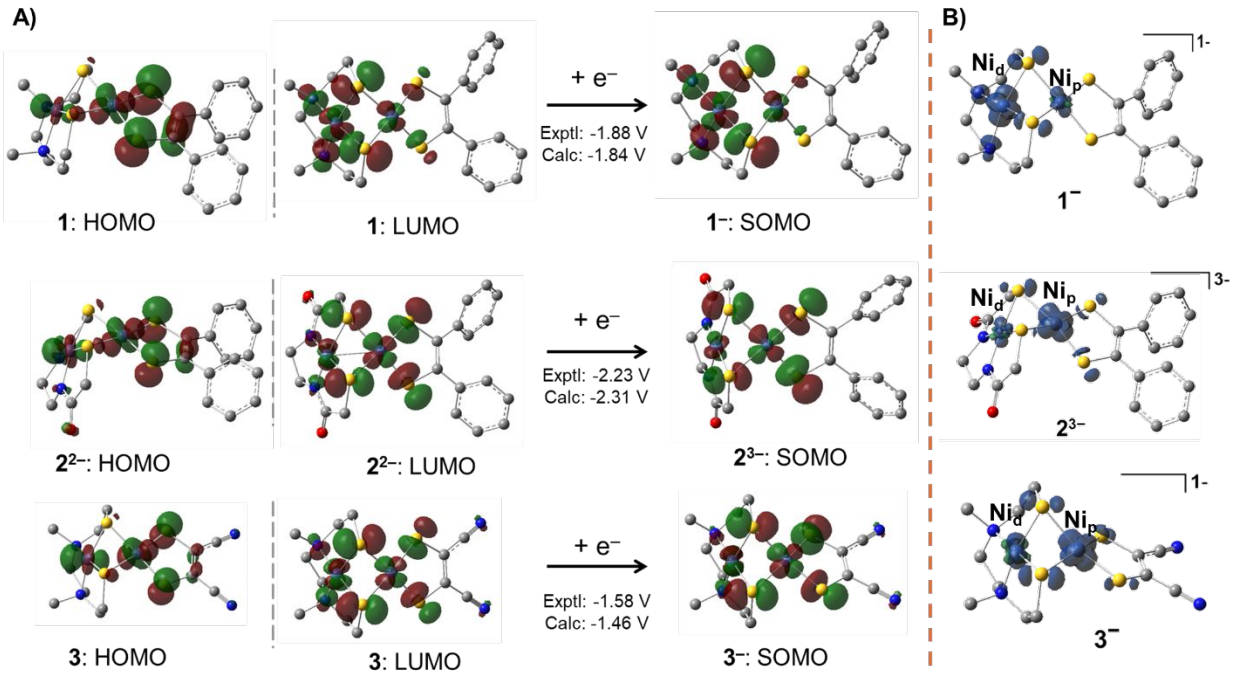

Figure 4. A) Frontier molecular orbitals (iso value = 0.04) of **1**, $\mathbf{2}^{2-}$, and **3** as isolated and reduced forms (**1**$^-$, $\mathbf{2}^{3-}$, and **3**$^-$). B) Spin Density plots for the reduced complexes **1**$^-$, $\mathbf{2}^{3-}$, **3**$^-$ (iso value = 0.001).

The calculated optimized structures and the experimental solid-state structures are in excellent agreement (see ESI **Table S4**). Additionally, the calculated reduction potentials for each complex matches well with the experimental values, **Table 2**, and **Figure 4A**. As discussed above, complex **3** lacks a dithiolene-based oxidation in the electrochemical window of our study, because of the electron-withdrawing cyano groups on the dithiolene ligand. Reduction of each complex yields paramagnetic doublet species. Spin density plots of these DFT optimized doublet species, **Figure 4A**, shows that majority of the unpaired spin density resides on Ni_d for $\mathbf{1}^-$ but on Ni_p for $\mathbf{2}^{3-}$ and $\mathbf{3}^-$. In all cases the spin density is consistent with the electron being added to a Ni-based d_{x2-y2} anti-bonding orbital, a conclusion that is consist with the LUMOs of the as-isolated complexes and in the SOMOs of the reduced forms, **Figure 4A**, although the orbitals are more delocalized on the ligands. The structural responses from reduction at each Ni are seen in distortions from square planarity, i.e., the τ_4 values given in **Table 2**. Reduction produces negligible τ_4 changes (maximum change is 0.06) at Ni1 for all complexes. Although complex **1** also shows negligible changes in τ_4 at Ni_p center, complexes $\mathbf{2}^{2-}$ and **3** show significant changes with the τ_4 value increasing from 0.07 and 0.08 to 0.20 and 0.31, respectively. The minimal structural changes for **1** and the significant changes for $\mathbf{2}^{2-}$ and **3** align well with the quasi-reversibility of the experimental reduction events for the former and the irreversibility of the latter complexes (**Figure 3**). Although the spin density shows the spin to be delocalized over Ni_d and Ni_p, complexes $\mathbf{2}^{2-}$ and **3** show higher spin density on Ni_p, which apparently has greater potential for structural flexibility. The site-specific reduction at Ni_p is analogous to the catalytic/redox active Ni_p in the ACS active site especially in complex $\mathbf{2}^{2-}$ which features a similar dianionic $Ni(N_2S_2)$ donor. Taken together, the DFT calculations are consistent with our assignment of the first reduction of these complexes as Ni_d based for **1** and Ni_p based for $\mathbf{2}^{2-}$ and **3**. Increasing the donor

strength of Ni_d, as in $\mathbf{2}^{2-}$, or the acceptor strength of Ni_p, as in **3**, moves the redox event from Ni_d, as in **1**, to Ni_p.

Table 2. Comparison of the theoretical and the experimental reduction potentials with concomitant structural changes (τ_4) at each nickel site upon reduction.

	$\mathbf{1}^{0/-}$	$\mathbf{2}^{2-/3-}$	$\mathbf{3}^{0/-}$
Exptl. E_{red} (V)	-1.88	-2.23	-1.58
Calc. E_{red} (V)	-1.84	-2.31	-1.46
Ni_d τ_4 (DFT opt. structures)	0.11 / 0.14	0.11 / 0.06	0.12 / 0.06
$Ni_p\tau_4$ (DFT opt. structures)	0.08 / 0.04	0.07 / 0.20	0.08 / 0.31

Chemical Oxidation of 1 and $\mathbf{2}^{2-}$

The fully reversible electrochemical oxidation events observed for **1** and $\mathbf{2}^{2-}$ prompted attempts to isolate the oxidized forms by bulk chemical means. Oxidation of **1** using [Fc][X] (X = $BArF_{24}^-$ or PF_6^-) in DCM at 23 °C results in an immediate color change from red to purple. Similar attempts for oxidation of $\mathbf{2}^{2-}$ resulted in insoluble green solids, likely due to decomposition. Multiple attempts at obtaining single crystals for SC-XRD analysis were unsuccessful. Our assumption of the identity of the product generated via oxidation of **1** was supported by EPR and UV-Vis spectroscopies.

The electronic absorption spectrum of the chemically oxidized, presumably $\mathbf{1}^+$**,** complex displays an intense band at 846 nm which is absent in the neutral complex **1**, **Figure 5A**. Additionally, a rhombic pattern in the EPR spectrum was observed for the frozen solutions of $\mathbf{1}^+$ (in CH_3CN/DCM 1:1 mixture) at 5 K, **Figure 5C**, with g values of 2.12, 2.04 and 1.99. The presence of such an intense low-energy band and the rhombic EPR pattern with g_{avg} = 2.05 are interpreted as oxidation at the nickel dithiolene unit generating a predominantly $[Ni(S_2C_2R_2)]^{+\bullet}$

radical monocation.[29-33] The spin density plot of complex $\mathbf{1}^+$ shows that the unpaired spin is mostly localized on the dithiolene ligand ($S_2C_2Ph_2$) group, with little contribution from the Ni_d and Ni_p atoms (**Figure 5D**). This result bolsters our assertion that the dithiolene ligand might mimic the 4Fe4S cluster of the ACS active site.

TD-DFT calculations of $\mathbf{1}^+$

To gain insight into the intense low energy absorption in complex $\mathbf{1}^+$, TD-DFT methods were executed using the M06-HF functional which has full Hartree−Fock exchange (see experimental section for details). The calculated excited state transitions included the 846 nm absorption band (see ESI **Figure S24**), finding a close match to the experimental data. From the TD-DFT results, the major contribution to 846 nm transition comes from the β HOMO to the β LUMO, shown in **Figure 5B**.

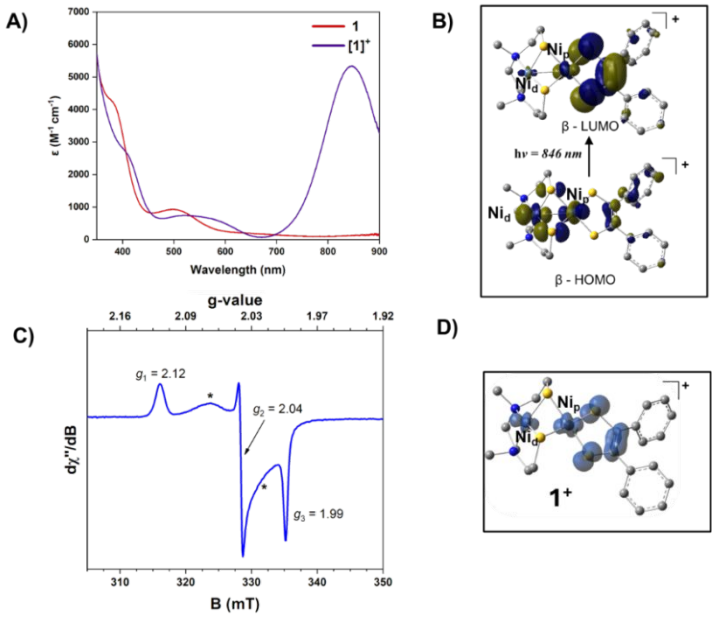

Figure 5. A) UV-Vis spectra of **1** and its oxidized form $\mathbf{1}^+$. B) The MOs involved (isovalue : 0.04) with the strong 846 nm absorption. C) CW-EPR spectra at 5 K for frozen solution of complex $\mathbf{1}^+$ in 1:1 DCM/MeCN mixture. D) Calculated spin density plot for $\mathbf{1}^+$ complex (isovalue : 0.0001).

Analysis of the β HOMO natural transition orbital (NTO) reveals that the electron density remains partially delocalized across the Ni_d-μ_2S_2-Ni_p core, which comprises of the $3d_z^2$ orbital of Ni_d, the $3d_{xz}$ orbital of Ni_p, and the bridging sulfur p-orbitals; this electron density is transferred to the LUMO comprised of the $(S_2C_2Ph_2)^{+\bullet}$ π^* system. This is attributed to metal to ligand charge transfer transition (MLCT). To our knowledge, sulfur-bridged bimetallics based on $M(N_2S_2)$ donors have not been seen to display such low energy transition features, i.e., bands resulting from electron density transfer across the bridging thiolates in the near IR region.

Conclusion

Site-specific redox events in bimetallic transition metal complexes offer characteristics that are readily related to enzyme active sites. Swings in electron density within our Ni-Ni' series are moderated by the ligand environment around each nickel and lead to site specific electron density "repositories". Within the electrochemical reaction range we find the reduction of complex **1** is $Ni(N_2S_2)$ based while reductions of complexes $\mathbf{2}^{2-}$ and **3** are nickel dithiolene based. This conclusion is ascribed to the electron-rich $[Ni(ema)]^{2-}$ dianionic donor in the former, and the electron-withdrawing cyano group on the dithiolene for the latter. Complex **1** features a reversible dithiolene based oxidation event, a conclusion that is supported by results from EPR spectroscopy. Furthermore, an intense band at 846 nm for $\mathbf{1}^+$ was observed that was absent in **1.** Charge transfer from the $Ni(N_2S_2)$ into the depleted dithiolene π-orbital accounts for this feature.

An intriguing aspect of our series is the identification of the dithiolene ligand as a charge reservoir, resembling the 4Fe4S cluster bridging to Ni_p in the ACS active site. The DFT calculations provide support for the redox assignments of each complex, revealing that complexes $\mathbf{2}^{2-}$ and **3** display structural alterations upon reduction, which aligns with the observed irreversible reductions, while complex **1** exhibits reversibility. From electrostatic potential (ESP) maps (see ESI, **Figure S23**) the electron rich regions in complexes **1** and $\mathbf{2}^{2-}$ are at the nickel dithiolene

sulfurs. Unfortunately, of sporadic reproducibility compound **1** was found to take up oxygen at the dithiolene sulfur site, forming a terminal sulfonated S-species detected by XRD on selected crystals.

These complexes present a unique platform to define the effects of the donor and receiver units on the redox properties of sulfur-bridged bimetallic complexes. Renewed interest in the ACS active site signifies the necessity for new model compounds in the development of catalysts that can valorize CO_2 into fuels.[34-36] Ongoing studies will leverage the knowledge obtained in this study towards bimetallic activation of small molecules.

Experimental Section

General Considerations.

The following solvents were purified by the MBraun Manual Solvent Purification System with AlcoaF200 activated alumina desiccant, acetonitrile (CH_3CN), dichloromethane (CH_2Cl_2), hexane, tetrahydrofuran (THF), and diethyl ether. Manipulations and reactions were carried out in anerobic conditions using standard Schlenk conditions under N_2 atmosphere or in a N_2 atmosphere glovebox. Unless otherwise stated, all reagents were used as received from standard vendors such as Sigma Aldrich, TCI, Ambeed, and BTC. The following ligands and complexes were made in house based on published procedures: *N*,*N*'-dimethyl-N,N'-bis(2-mercaptoethyl)ethylenediamine (H_2bme-dame), *N*,*N'*-ethylenebis(2-mercaptoacetamide) (H_4ema) [Fc][BArF], Ni(bme-dame), $[Ni(ema)][NEt_4]_2$, $Ni(mnt)(CNMe)_2$, and $Ni(dpdt)(CNMe)_2$.[37-40] Ethanol (EtOH) was degassed and dried with 3 Å molecular sieves prior to use. Acetone was simply purged with N_2 for 15 mins prior to dissolving the starting materials. The supporting electrolyte [n-Bu_4N][PF_6] and $AgBF_4$ were reagent grade and purchased from Sigma-Aldrich.

Physical measurements.

Bruker 400 MHz systems were used to record ^{1}H NMR and ^{13}C NMR spectra. Infrared spectra were recorded on the Bruker Tensor 37 Fourier transform IR (FTIR) spectrometer using a CaF_2 cell with 0.2 mm path length. Mass spectrometry (ESI-MS) was performed at the laboratory for Biological Mass Spectrometry at Texas A&M University. EPR spectra of $[NiNi']^{+}$ were recorded on a continuous wave (CW) X-band (9.39 GHz) ELEXSYS spectrometer as a frozen glass (DCM:CH_3CN / 1:1). EPR parameters were as follows: temperature 4 K; 9.382 GHz microwave frequency; 1 G modulation amplitude; 100 kHz modulation frequency; 40 ms conversion time; 632 mW microwave power. Elemental analyses were performed at the Atlantic Microlab Inc., located in Norcross, Ga.

X-ray Structure Determination.

The crystal structures of **1**, $\mathbf{2}^{2-}$ and **3** were determined using BRUKER Quest X-ray (fixed-Chi geometry) diffractometer at 110 K with a Mo-Iμs X-ray tube (K_α = 0.71073 Å). Integrated intensity information for each reflection was obtained by reduction of the data frames with the program APEX3.[41] The data was merged and scaled to produce a suitable data set. The absorption correction program SADABS was employed to correct the data for absorption effects.[42] Solutions were obtained readily using XT/XS in APEX3.[43,44] Hydrogen atoms were placed in idealized positions and were set riding on the respective parent atoms. All non-hydrogen atoms were refined with anisotropic thermal parameters. Absence of additional symmetry or void were confirmed using PLATON (ADDSYM).[45] The structure was refined (weighted least squares refinement on F^2) to convergence using Olex2.[46]

Electrochemistry.

Cyclic voltammograms were recorded using the CHI600E electrochemical analyzer (CH instruments, Inc.) in a three-electrode cell. Measurements were carried out under anerobic conditions at room temperature using CH_3CN as solvent with 0.1 M $[^tBu_4N][PF_6]$ as the electrolyte and 1.0 mM of analyte (0.4 mM for **3**). Platinum wire as the counter electrode, 0.071 cm^2, a glassy carbon disk was used as the working electrode, and the reference electrode was a CH_3CN solution of $Ag/AgNO_3$ in a Vycor-tipped glass tube. All potentials were referenced to the Fc^+/Fc redox couple at 0.00 V. For polishing the working electrode an alumina-water slurry was used with a positive pressure of N_2 when removing or reinserting the electrode.

Synthesis.

Ni(bme-dame)-Ni(dpdt), **1**. Reactants Ni(bme-dame) (66 mg, 0.25 mmol) and $Ni(dpdt)(CNMe)_2$ (76 mg, 0.2 mmol) were refluxed in EtOH for 24 h under N_2. The resulting maroon precipitate was washed with EtOH and diethyl ether. The solids were then dissolved in DMF and filtered through a small celite plug. Ether was added to precipitate out the complex as maroon solid (Yield: 79 mg, 70 %). Dark red X-ray quality crystals of **1** were grown in CH_2Cl_2/hexane at −35 °C. ^1H NMR (CD_2Cl_2): δ 2.33 (m, 2.09), 2.43 (m, 2.00), 2.63 (s, 6.00), 2.77 (m, 3.90) 3.77 (q, 2.05), 4.85 (t, 2.21), 7.09 (m, 5.97) 7.19 (m, 3.86). UV-vis absorption spectrum [CH_3CN, λ_{max}, nm (ε_M, M^{-1} cm^{-1}.)]: 660 115), 500 (930), 380 (4240). ESI-MS positive mode: $[M] - e^- = 563.9841$ m/z (calculated 563.9837 m/z). Anal. Calcd for $H_{28}C_{22}N_2S_4Ni_2$ 0.5•(CH_2Cl_2, C_3H_7NO): H, 5.08; C, 44.68; N, 5.43. Found: H, 4.95; C, 44.93; N, 5.35.

[Ni(ema)-Ni(dpdt)][NEt$_4$]$_2$, $\mathbf{2}^{2-}$. In separate vials, 52 mg (0.10 mmol) of $[Ni(ema)]^{2-}$ and 42 mg (0.11 mmol) of $Ni(dpdt)(CNMe)_2$ were dissolved in minimum amount of acetonitrile. The

$Ni(dpdt)(CNMe)_2$ solution was added to the $[Ni(ema)]^{2-}$ solution dropwise and stirred for 15 min at room temperature, generating a dark red solution. Ether was then added and stirred for 5 min to precipitate out the product. After Et_2O/CH_3CN mixture was removed, the precipitated product was washed 3 times with THF and then dried. This procedure afforded 60 mg (73%) of product as a dark red solid. The $\mathbf{2}^{2-}$ product was then redissolved in acetonitrile, layered with ether, and stored in -35°C to develop red X-ray quality crystals. ^1H NMR (CH_3CN): δ 2.47 (d, 1.29), 2.86 (m, 5.03), 3.34 (m, 2.30), 7.06 (m, 10). UV-vis absorption spectrum [CH_3CN, λ_{max}, nm (ε_M, M^{-1} cm^{-1})]: 555 (1600), 422 (4110). ESI-MS positive mode: $[M]^{2-} - e^- = 561.8966$ m/z (calculated 561.8956 m/z). Anal. Calcd for $H_{58}C_{36}N_4O_2S_4Ni_2$: H, 7.09; C, 52.44; N, 6.80. Found: H, 7.06; C, 49.06; N, 7.36.

Ni(bme-dame)-Ni(mnt), **3**. Reactants Ni(bme-dame) (66 mg, 0.25 mmol) and $Ni(mnt)(CNMe)_2$ (56 mg, 0.2 mmol) were stirred at 23 °C in acetone for 24 h. The resulting red precipitate was separated from the acetone reaction mixture and washed twice with 5 mL of acetone. Filtration through a small celite plug was then performed by using DMSO as the solvent (Yield: 46 mg, 50 %). Dark red X-ray quality crystals of **3** were grown in DMSO layered with a 50/50 mixture of H_2O/MeOH at 23 °C. ^1H NMR (DMSO): δ 2.08 (s, 0.99), 2.93 (t, 2.13), 3.19 (s, 6.00), 3.70 (s, 2.01), 3.90 (s, 3.75), 4.27 (s, 1.95), 4.44 (t, 1.98). UV-vis absorption spectrum [CH_3CN, λ_{max}, nm (ε_M, M^{-1} cm^{-1})]: 500 (1230), 392 (5880), 367 (6700). ESI-MS negative mode: $[M] + Cl^- = 496.8776$ m/z (calculated 496.8775 m/z). Anal. Calcd for $H_{12}C_{18}N_4S_4Ni_2$: H, 3.91; C, 31.07; N, 12.08. Found: H, 3.84; C, 30.85; N, 11.80.

Computational methodology. Density functional theory (DFT) calculations were performed in Gaussian 16 Revision B.0109[47] with the TPSS[48] functional. Triple-ζ basis set 6-311++G(d,p) was used for hydrogen, carbon, sulfur, nitrogen, and oxygen,[49-51] while the Wachters-Hay basis set, 6-311++G(d,p)[52-54] was used for nickel. The crystal structure of **1**, $\mathbf{2}^{2-}$ and **3** were imported to use as

the starting coordinates for gas phase optimization and frequency calculations using GaussView 6.0.16.17.[55] Since no crystal structure are available for $\mathbf{1}^{-}$, $\mathbf{2}^{3-}$, and $\mathbf{3}^{-}$, the optimal geometries of singlets **1**, $\mathbf{2}^{2-}$ and **3** were used as the initial geometries, respectively, for optimizations. Likewise, the initial geometry of $\mathbf{1}^{+}$ for optimization was based on the optimal geometry of singlet **1**. All species were confirmed to be minimum energy structures by the absence of imaginary frequencies. Thermal corrections and solvation corrections (with SMD model, in acetonitrile)[56] were added to calculate Gibbs free energy. Time-dependent density functional theory (TD-DFT)[57-62] calculations were performed on the optimized structure of $\mathbf{1}^{+}$ using the global hybrid M06-HF functional,[63] along with the same basis set mentioned above. The first 45 excited states were calculated using the SMD model with acetonitrile as the solvent, and spectral simulations were constructed by broadening the optical transitions by the Gaussian function with a width of σ = 0.2 eV. The calculated standard reduction potentials E (vs. $Fc^{+/0}$) shown in **Table 2** were calculated by the following equation:

$$E = -\frac{G(Red) - G(Ox) + G(Fc+) - G(Fc)}{nF}$$

Where G is the calculated Gibbs free energy, n is the equivalents of electrons transferred, F is the Faraday constant.

Conflicts of Interest

The authors declare no conflicts of interest.

Acknowledgements

We gratefully acknowledge the financial support of the National Science Foundations (MPS CHE 2102159) and the Robert A. Welch Foundation (A-0924) for synthesis and general characterization of the complexes. Experimentation related to low temperature Continuous-Wave Electron Paramagnetic Resonance measurements was supported as part of the Reconfigurable Materials

Inspired by Nonlinear Neuron Dynamics (REMIND) Energy Frontier Research Center, funded by the U.S. Department of Energy (DOE), Office of Science, Basic Energy Sciences (BES), under award *#DE-SC0023353*.

References

1 D. E. Herbert, D. Lionetti, J. Rittle and T. Agapie, *J. Am. Chem. Soc.*, 2013, **135**, 19075–19078.

2 G. de Ruiter, N. B. Thompson, D. Lionetti and T. Agapie, *J. Am. Chem. Soc.*, 2015, **137**, 14094–14106.

3 S. E. Creutz and J. C. Peters, *J. Am. Chem. Soc.*, 2015, **137**, 7310–7313.

4 N. X. Gu, G. Ung and J. C. Peters, *Chem. Commun.*, 2019, **55**, 5363–5366.

5 D. Singh, W. R. Buratto, J. F. Torres and L. J. Murray, *Chem. Rev.*, 2020, **120**, 5517–5581.

6 P. Gandeepan, T. Müller, D. Zell, G. Cera, S. Warratz and L. Ackermann, *Chem. Rev.*, 2019, **119**, 2192–2452.

7 M. V. Rampersad, S. P. Jeffery, J. H. Reibenspies, C. G. Ortiz, D. J. Darensbourg and M. Y. Darensbourg, *Angew. Chem. Int. Ed.*, 2005, **44**, 1217–1220.

8 C. Darnault, A. Volbeda, E. J. Kim, P. Legrand, X. Vernède, P. A. Lindahl and J. C. Fontecilla-Camps, *Nat. Struct. Mol. Biol.*, 2003, **10**, 271–279.

9 M. Can, F. A. Armstrong and S. W. Ragsdale, *Chem. Rev.*, 2014, **114**, 4149–4174.

10 R. E. Treviño and H. S. Shafaat, *Curr. Opin. Chem. Biol.*, 2022, **67**, 102110.

11 H. S. Shafaat, A. C. Manesis and A. Yerbulekova, *Acc. Chem. Res.*, 2023, **56**, 984–993.

12 J. A. Denny and M. Y. Darensbourg, *Chem. Rev.*, 2015, **115**, 5248–5273.

13 M. Quiroz, M. M. Lockart, M. R. Saber, S. W. Vali, L. C. Elrod, B. S. Pierce, M. B. Hall and M. Y. Darensbourg, *Proc. Natl. Acad. Sci. U.S.A.*, 2022, **119**, e2201240119.

14 W. G. Dougherty, K. Rangan, M. J. O'Hagan, G. P. A. Yap and C. G. Riordan, *J. Am. Chem. Soc.*, 2008, **130**, 13510–13511.

15 M. Ito, M. Kotera, T. Matsumoto and K. Tatsumi, *Proc. Natl. Acad. Sci. U.S.A.*, 2009, **106**, 11862–11866.

16 V. Mathrubootham, J. Thomas, R. Staples, J. McCraken, J. Shearer and E. L. Hegg, *Inorg. Chem.*, 2010, **49**, 5393–5406.

17 F. Osterloh, W. Saak and S. Pohl, *J. Am. Chem. Soc.*, 1997, **119**, 5648–5656.

18 A. Obanda, K. Martinez, R. H. Schmehl, J. T. Mague, I. V. Rubtsov, S. N. MacMillan, K. M. Lancaster, S. Sproules and J. P. Donahue, *Inorg. Chem.*, 2017, **56**, 10257–10267.

19 K. Arumugam, M. Selvachandran, A. Obanda, M. C. Shaw, P. Chandrasekaran, S. L. Caston Good, J. T. Mague, S. Sproules and J. P. Donahue, *Inorg. Chem.*, 2018, **57**, 4023–4038.

20 H. J. Kruger, G. Peng and R. H. Holm, *Inorg. Chem.*, 1991, **30**, 734–742.

21 E. R. Hosler, R. W. Herbst, M. J. Maroney and B. S. Chohan, Dalton Trans., 2011, 41, 804–816.

22 B. S. Lim, D. V. Fomitchev and R. H. Holm, *Inorg. Chem.*, 2001, **40**, 4257–4262.

23 R. Eisenberg and H. B. Gray, *Inorg. Chem.*, 2011, **50**, 9741–9751.

24 M. V. Rampersad, S. P. Jeffery, M. L. Golden, J. Lee, J. H. Reibenspies, D. J. Darensbourg and M. Y. Darensbourg, *J. Am.Chem. Soc.*, 2005, **127**, 17323–17334.

25 C.-H. Hsieh, S. Ding, Ö. F. Erdem, D. J. Crouthers, T. Liu, C. C. L. McCrory, W. Lubitz, C. V. Popescu, J. H. Reibenspies, M. B. Hall and M. Y. Darensbourg, *Nat Commun*, 2014, **5**, 3684.

26 S. M. Brothers, M. Y. Darensbourg and M. B. Hall, *Inorg. Chem.*, 2011, **50**, 8532–8540.

27 P. Ghosh, S. Ding, R. B. Chupik, M. Quiroz, C.-H. Hsieh, N. Bhuvanesh, M. B. Hall and M. Y. Darensbourg, *Chem. Sci.*, 2017, **8**, 8291–8300.

28 S. Ding, P. Ghosh, M. Y. Darensbourg and M. B. Hall, *Proceedings of the National Academy of Sciences*, 2017, **114**, E9775–E9782.

29 P. Machata, P. Herich, K. Lušpai, L. Bucinsky, S. Šoralová, M. Breza, J. Kozisek and P. Rapta, *Organometallics*, 2014, **33**, 4846–4859.

30 A. Begum, G. Moula and S. Sarkar, *Chem. Eur. J.*, 2010, **16**, 12324–12327.

31 A. Kochem, T. Weyhermüller, F. Neese and M. van Gastel, *Organometallics*, 2015, **34**, 995–1000.

32 K. Ray, T. Weyhermüller, F. Neese and K. Wieghardt, *Inorg. Chem.*, 2005, **44**, 5345–5360.

33 Q. Miao, J. Gao, Z. Wang, H. Yu, Y. Luo and T. Ma, *Inorganica Chim. Acta*, 2011, **376**, 619–627.

34 M. Can, M. J. Abernathy, S. Wiley, C. Griffith, C. D. James, J. Xiong, Y. Guo, B. M. Hoffman, S. W. Ragsdale and R. Sarangi, *J. Am. Chem. Soc.*, 2023, **145**, 13696-13708.

35 H. S. Shafaat and J. Y. Yang, *Nat. Catal.*, 2021, **4**, 928–933.

36 S. Gencic, E. C. Duin and D. A. Grahame, *J. Inorg. Biochem.*, 2023, **240**, 112098.

37 K. D. Karlin and S. J. Lippard, *J. Am. Chem. Soc.*, 1976, **98**, 6951–6957.

38 N. G. Connelly and W. E. Geiger, *Chem. Rev.*, 1996, **96**, 877–910.

39 E. Bouwman, R. K. Henderson, A. L. Spek and J. Reedijk, *Eur. J. Inorg. Chem.*, 1999, **1999**, 217–219.

40 N. G. Connelly, J. G. Crossley and A. G. Orpen, *J. Chem. Soc., Chem. Commun.*, 1992, 1568–1571.

41 APEX3 “Program for Data Collection on Area Detectors” BRUKER AXS Inc., 5465 East Cheryl Parkway, Madison, WI 53711-5373 USA.

42 SADABS, G. M. Sheldrick, “Program for Absorption Correction of Area Detector Frames”, BRUKER AXS Inc., 5465 East Cheryl Parkway, Madison, WI 53711-5373 USA.

43 G. M. Sheldrick, *Acta Cryst. A*, 2015, **71**, 3–8.

44 G. M. Sheldrick, *Acta Cryst. C*, 2015, **71**, 3–8.

45 A. L. Spek, *J. Appl. Cryst.*, 2003, **36**, 7–13.

46 O. V. Dolomanov, L. J. Bourhis, R. J. Gildea, J. a. K. Howard and H. Puschmann, *J. Appl. Cryst.*, 2009, **42**, 339–341.

47 Gaussian 16, Revision C.01, M. J. Frisch, G. W. Trucks, H. B. Schlegel, G. E. Scuseria, M. A. Robb, J. R. Cheeseman, G. Scalmani, V. Barone, G. A. Petersson, H. Nakatsuji, X. Li, M. Caricato, A. V. Marenich, J. Bloino, B. G. Janesko, R. Gomperts, B. Mennucci, H. P. Hratchian, J. V. Ortiz, A. F. Izmaylov, J. L. Sonnenberg, D. Williams-Young, F. Ding, F. Lipparini, F. Egidi, J. Goings, B. Peng, A. Petrone, T. Henderson, D. Ranasinghe, V. G. Zakrzewski, J. Gao, N. Rega, G. Zheng, W. Liang, M. Hada, M. Ehara, K. Toyota, R. Fukuda, J. Hasegawa, M. Ishida, T. Nakajima, Y. Honda, O. Kitao, H. Nakai, T. Vreven, K. Throssell, J. A. Montgomery, J. E. Peralta, F. Ogliaro, M. J. Bearpark, J. J. Heyd, E. N. Brothers, K. N. Kudin, V. N. Staroverov, T. A. Keith, R. Kobayashi, J. Normand, K. Raghavachari, A. P. Rendell, J. C. Burant, S. S. Iyengar, J. Tomasi, M. Cossi, J. M. Millam, M. Klene, C. Adamo, R. Cammi, J. W. Ochterski, R. L. Martin, K. Morokuma, O. Farkas, J. B. Foresman, D. J. Fox, Gaussian, Inc., Wallingford CT, 2016.

48 J. Tao, J. P. Perdew, V. N. Staroverov and G. E. Scuseria, *Phys. Rev. Lett.*, 2003, **91**, 146401.

49 R. Krishnan, J. S. Binkley, R. Seeger and J. A. Pople, *J. Chem. Phys.*, 1980, **72**, 650–654.

50 A. D. McLean and G. S. Chandler, *J. Chem. Phys.*, 1980, **72**, 5639–5648.

51 T. Clark, J. Chandrasekhar, G. W. Spitznagel and P. V. R. Schleyer, *J. Comput. Chem.*, 1983, **4**, 294–301.

52 A. J. H. Wachters, *J. Chem. Phys.*, 1970, **52**, 1033–1036.

53 P. J. Hay, *J. Chem. Phys.*, 1977, **66**, 4377–4384.

54 K. Raghavachari and G. W. Trucks, *J. Chem. Phys.*, 1989, **91**, 1062–1065.

55 GaussView, Version 6, R. Dennington, T. A. Keith, J. M. Millam, Semichem Inc., Shawnee Mission, KS, 2016.

56 A. V. Marenich, C. J. Cramer and D. G. Truhlar, *J. Phys. Chem. B*, 2009, **113**, 6378–6396.

57 R. Bauernschmitt and R. Ahlrichs, *Chemical Physics Letters*, 1996, **256**, 454–464.

58 M. E. Casida, C. Jamorski, K. C. Casida and D. R. Salahub, *J. Chem. Phys.*, 1998, **108**, 4439–4449.

59 F. Furche and R. Ahlrichs, *J. Chem. Phys.*, 2002, **117**, 7433–7447.

60 R. E. Stratmann, G. E. Scuseria and M. J. Frisch, *J. Chem. Phys.*, 1998, **109**, 8218–8224.

61 C. Van Caillie and R. D. Amos, *Chem. Phys. Lett.*, 1999, **308**, 249–255.

62 C. Van Caillie and R. D. Amos, *Chem. Phys. Lett.*, 2000, **317**, 159–164.

63 Y. Zhao and D. G. Truhlar, *J. Phys. Chem. A*, 2006, **110**, 13126–13130.